J Mater Sci (2012) 47:720–729
DOI 10.1007/s10853-011-5845-5

Effect of tempering treatment on microstructure and fatigue life of TiC–Cr overlay, produced by plasma transferred arc alloying

Kaiyuan Shi · Shubing Hu · Lingjiang Liang

Received: 6 July 2011 / Accepted: 2 August 2011 / Published online: 11 August 2011

Abstract In this work, TiC–Cr overlay formed by plasma transferred arc alloying was subjected to tempering treatment at 473, 673, and 873 K for 2 h, respectively. XRD was employed to investigate phase transformation, determine the austenite proportion and evaluate the crystallite size. Microstructure investigation by SEM and TEM, microhardness and fatigue test were performed on as-deposited condition and after tempering. Evolution of microstructure as well as its relationship with microhardness and fatigue property of coating was described. The results suggest that both microhardness and fatigue strength could be improved by tempering at 473 K; however, further elevation of the temperature directs degradation. Based on the Weibull distribution, tempering treatment increases the slope of fitting line, which suggests that fatigue life becomes more predictable.

Introduction

During the last years, the materials demand gave rise to an important improvement in the techniques to modify surface. High energy beam alloying like laser, electron beam, and plasma transferred arc (PTA) is one of the techniques, which have been generally used. Although the hardness [1–4], wear resistance [5–7] erosion resistance [8, 9] could be increased by selecting appropriate alloying material and optimizing processing parameters, there was a common problem existed that the alloying overlay represented a state of high residual stress, low toughness, and poor ductile [10–12]. For industrial-utilized components which served in the life range from 10^2 to 10^6 cycles, fatigue property after alloying should be highly considered. In order to get a well combination of microstructure and fatigue strength, tempering is an attractive option for the reason that it is a convenient and could proceed by a sequence of structural changes, including recovery of the dislocation and precipitation of carbides [13–17].

Various research works have been focused on the effect of subsequent heat treatment on alloying sample. Beaurin et al. [18], in the working on influence of subsequent heat treatment durations, reported that the microstructure of alloying sample was not significantly affected by a short time treatment whereas changes were observed for longer durations, although hardness remains almost unchanged. Li et al. [19] studied the heat treatment on mechanical properties of PTA alloying by nano-indentation test. They concluded that hardness and elastic modulus of subsequent heat-treated coatings were generally lower than those of as-alloying conditions as a result of the dissolution of the eutectic structure which decreased the effect of dispersion strengthening. Wu et al. [20] used TEM to verify that in situ carbide transformations of primary M_7C_3 to $M_{23}C_6$ and eutectic M_7C_3 to M_6C, respectively, occurred in alloying zone (AZ) during tempering. Similar observations on the topology and morphology of secondary carbide precipitation were made by Zhang et al. [21] and Wang et al. [22], they studied the phase transformation of Fe-based alloying coating and proposed the evolution sequence of the phase

K. Shi (✉) · S. Hu (✉) · L. Liang
State Key Laboratory of Material Processing and Die & Mould Technology, Huazhong University of Science & Technology, Wuhan 430074, China
e-mail: hustclsky@qq.com

S. Hu
e-mail: hushubing@163.com

with the elevation of temperature as follows: $L \rightarrow \gamma + L \rightarrow \gamma + (\gamma + (Cr,Fe)_7C_3) \rightarrow (\gamma + (Cr,Fe)_{23}C_6 + \alpha)$.

The vast majority of experimental efforts have applied to the transformation of the microstructure and the morphology of the precipitation at the AZ, and there were still many unexplored points such as beside the hardness, other properties after tempering were seldom investigated. And most investigations were based on the subsequent treatment study of laser alloying, very limited literature was available on PTA even though its advantages are well established [1, 2]. Therefore, in the present work, we carried out different tempering temperatures on PTA alloying TiC–Cr to explore for a close control of the microstructure and fatigue property. The effort was focused on not only calculating phase volume fraction variation of AZ, but also discussing the microstructure transformation of heat affected zone (HAZ). In addition, the effect of tempering on fatigue life was studied by Weibull distribution plots.

Experimental

Experimental material

For this work, a low-alloyed gray cast iron code named HT200 was used. It was obtained from the casting of a failed bower with a chemical composition shown in Table 1. The TiC powder and Cr powder were selected as alloying materials in the ratio of 7:3 (wt%). Before blending, the sizes of TiC powder and Cr powder were ranged from 2 to 20 μm and 50 to 120 μm, respectively. And steel balls were fed into the mixing jar to increase uniformity of the powders, which were mixed for 24 h.

Sample preparation and fatigue investigation

Experimental samples of 180 mm length, 30 mm width and 3 mm thickness were cut by electric spark machine. The PTA alloying was prepared by a self-designed PTA surface modification machinery on both sides with the arc traversing in a direction perpendicular to fatigue crack growth, and the operating parameters as well as schematic of modification process were given in elsewhere [23, 24]. After the PTA alloying, the specimens were classified into four groups. The first remained the original status, while other three groups were subjected to the tempering treatment at 473, 673, and 873 K separately (heated at 10 K/min to the temper temperature, holding for 2 h before air-cooling down to ambient temperature).

Table 1 Chemical composition of HT200 gray cast iron (wt%)

Compositions	C	Si	Mn	P	S	Cu	Cr	Fe
Content	3.250	1.570	0.920	0.060	0.059	0.500	0.270	Bal.

To study the effect of tempering on fatigue life, eight samples for each category were prepared, employed as single cracked edge tension (SECT) specimens. Its configuration is shown in Fig. 1. The experiment was carried on the closed-loop servo-hydraulic mechanical test machines, which had a capacity of 98 kN under computer control. All specimens were tested in laboratory air at the room temperature and relative humidity 40–50%. A constant stress amplitude ($R = 0.1$) and a sinusoidal load of frequency 10 Hz were applied throughout this study.

Characterization of temper effect

The temper effect on microstructure, microhardness, and phase transformation was studied under the following procedures. Transverse sections of different groups were cut parallel to the length direction, and standard methods of metallography were followed. The microstructure and element distribution were examined by Quanta 200 scanning electronic microscope (SEM). X-ray diffraction (XRD) was carried out to identify phase transformation with Cu Kα standard ($\lambda = 1.5403$ Å) radiation at the scanning speed of 0.3°/min on PANalytical X'Pert PRO diffractometer. The thin foils prepared for transmission electron microscope (TEM) observation were cut from the top of the AZ, and polished by mechanical grinding to 50 μm, then followed by ion milling at an angle of 10° under a voltage of 5.5 kV. TEM was carried out by a Tecnai G2 20 transmission electron microscope. Besides, a Vickers Micro-hardness Tester (DHV-1000, manufactured by Shanghai Shangcai Tester machine Co. Ltd, China) was used for the microhardness measurement.

Measurement of the volume fraction of the retained austenite and crystallite size

In this contest, the volume fraction of austenite (γ-Fe) as well as the sum of ferrite (α-Fe) and martensite (M) in the AZ was characterized by XRD, based on analysis of the

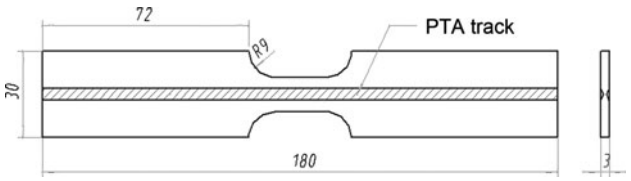

Fig. 1 Configuration of specimens employed for fatigue life study

$\alpha/M_{(110)}$ and $\gamma_{(111)}$ diffraction peaks, according to the following Eq. 1 [17]:

$$V_\gamma = \frac{1 - \mathrm{CVF}}{1 + K\left(I_{\alpha/\mathrm{M}(110)}/I_{\gamma(111)}\right)} \times 100\% \quad (1)$$

where V_γ, volume fraction of the retained austenite, CVF carbide volume fraction which can be obtained by image analysis using Photoshop and Image-Pro-Plus, according to Ref. [25]; $I_{\alpha/\mathrm{M}(110)}$ and $I_{\gamma(111)}$, the integrated intensity of α-Fe/martensite and austenite diffraction peaks; K, the scale factor that can be obtained using the following equations [26, 27]:

$$R_{\alpha/\mathrm{M},\gamma} = \frac{1}{v^2}\left[|F|^2 P\left(\frac{1+\cos^2 2\theta}{\sin^2\theta\cos\theta}\right)\right]\left(\frac{e^{-2M}}{2\mu}\right) \quad (2)$$

$$K = \frac{R_\gamma}{R_{\alpha(\mathrm{M})}} \quad (3)$$

where v is the unit cell volume of the certain phase, F is the structure factor, P is the multiplicity, θ is the angle of the peak, μ is the coefficient of absorption, and e^{-2M} is the Debye–Waller temperature factor. The ratio of $I_{\alpha/\mathrm{M}(110)}/I_{\gamma(111)}$ and the scale factor K for each category are shown in Table 2. And the volume fraction satisfies the following relationship:

$$\mathrm{CVF} + V_\gamma + V_{\alpha/\mathrm{M}} = 1 \quad (4)$$

Moreover, based on the XRD pattern, the true integral breadth (β) of each XRD peak profile was elevated after correcting for the Debye–Waller factor at that particular temperature and also for the instrumental broadening contribution [13]. The Scherrer equation was used to calculate the crystallite size (D_s) [28]:

$$D_s = \frac{K\lambda}{\beta\cos\theta} \quad (5)$$

where K is Scherrer constant (0.89 in this study), λ is X-ray wavelength, and θ is the reflection angle of the peak.

Results and discussion

Microstructure

The cross-section morphology of the harden layer produced by PTA alloying TiC–Cr is illustrated in Fig. 2. The overlay has a good metallurgical bond with the matrix by molten pool, having a thickness of 0.3–0.5 mm and free of cracks as well as porosities. The microstructural feature of PTA alloying overlay has two obvious boundaries which separate the cross-section into three zones: AZ, HAZ, and matrix.

Table 2 The ratio of $I_{\alpha/\mathrm{M}(110)}/I_{\gamma(111)}$ as well as the value of K between $I_{\alpha/\mathrm{M}(110)}$ and $I_{\gamma(111)}$

Tempered temperature	Untreated	473 K	673 K	873 K
$I_{\alpha/\mathrm{M}(110)}/I_{\gamma(111)}$	0.6391	1.0191	1.5553	–
K	0.7732	0.7737	0.7785	0.7798

Effect of tempering temperature on microstructural development of AZ

The transformation of AZ's microstructure between PTA alloying and subsequent heat treatment is illustrated in Fig. 3. Figure 3a shows the non-heat treatment microstructure, which consists of primary retained austenite, martensite, a large number of precipitations (bright spots) and a eutectic of $(Fe,Cr)_7C_3$ carbide (dark spots) and retained austenite. TEM (Fig. 4) confirms that the uniformly distributed precipitation (bright spots) is TiC, having a FCC crystal structure with a lattice parameter $a = 0.43$ nm, consistent with Lin's literature [29]. A mass of retained austenite cell was attributed to high content of alloying elements and carbon that can decrease the martensite start temperature M_s and inhibit pearlite formation [30]. Temper of the PTA alloying samples at 473 K has caused drastic changes in the austenite cell. Figure 3b depicts that the resulting microstructure is a great amount of needles like tempered martensitic structure formed within the primary retained austenite cell. The eutectic mixture of $(Fe,Cr)_7C_3$ and retained austenite remained at AZ, which implied that the energy such temperature offered was not sufficient to encourage formation of new carbide or the transformation into new carbides phases. However, after being tempered at 673 K (Fig. 3c), the

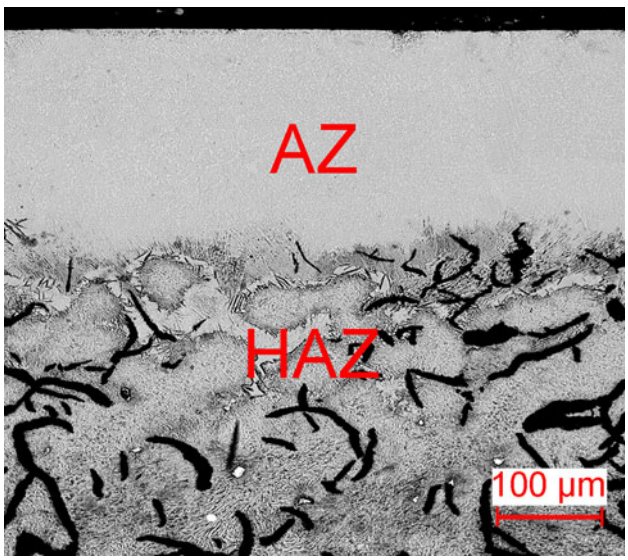

Fig. 2 Cross-section morphology of PTA alloying

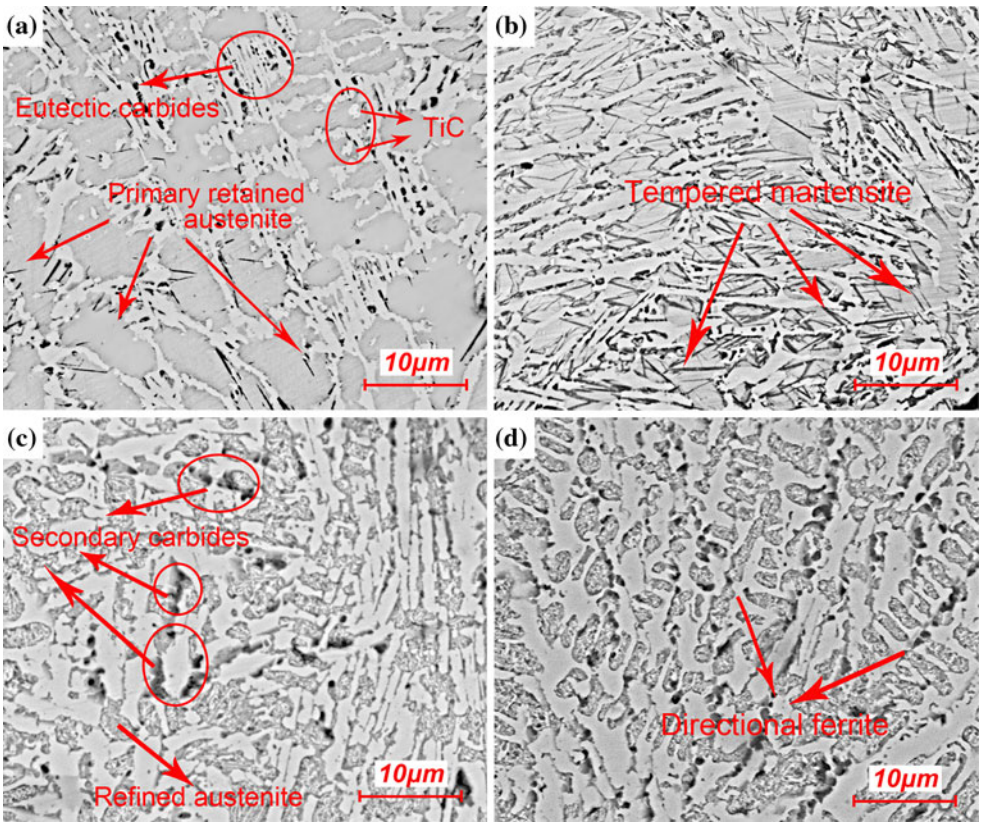

Fig. 3 Microstructure of AZ: **a** PTA alloyed, **b** tempered at 473 K, **c** tempered at 673 K, **d** tempered at 873 K

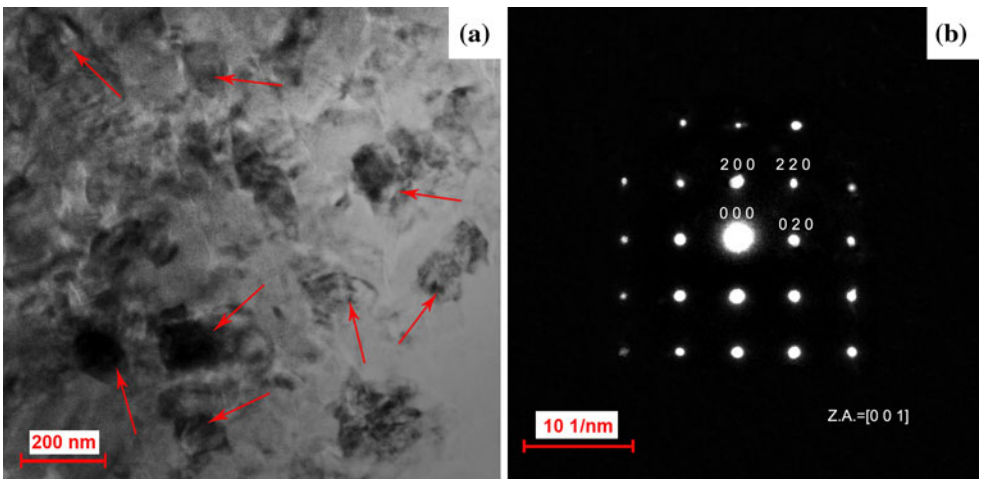

Fig. 4 TEM observation of TiC (**a**) and its corresponding electron diffraction (**b**)

eutectic mixture is partially decomposed and the austenite cell is further refined accompanied by formation of $(Fe,Cr)_{23}C_6$ secondary carbides at the boundary. The observation was compatibility with the research of Wu [20] and Zhang [21]. Powell [31] explained the thermodynamically unfavorable formation of $M_{23}C_6$ in terms of crystallographic matching between the lattice parameters of the carbide and the cubic matrix crystal structure. Such a matching lowers the activation energy that is essential for nucleation and, thus, reduces the overall involved surface energy. The magnification of the AZ microstructure after 843 K tempered showed that the non-directional refined austenite cell structure (Fig. 3c) changes into directional continuous grained ferrite (Fig. 3d). The dissolution of high carbon enriched retained austenite caused further participating and growing of $(Fe,Cr)_{23}C_6$ secondary

carbides. Through the analysis of the images of AZ, carbide proportion can be obtained, as shown in Table 3. The uncertainty of the carbide volume fraction is the statistical error of n which is the times of measurement in different regions of the sample. Considering a normal distribution, the error is calculated by using the following equation, which has been suggested in Refs. [32, 33]:

$$\Delta \mathrm{CVF} = \pm 3\frac{\sigma}{\sqrt{n-1}}(90\%\ \text{of confidence}) \quad (6)$$

where σ is standard deviation and n is the number of quantification.

XRD analysis of AZ (Fig. 5) confirms the presence of TiC, $(Fe,Cr)_7C_3$, martensite and a considerable amount of of γ-Fe. After tempering treatment, α-Fe and $(Fe,Cr)_{23}C_6$ were produced. By comparison, the peak intensities of γ-Fe after subsequent tempering treatment becomes weaker than the un-treated; at the same time, the peak intensities of α-Fe/martensite gradually increases and $(Fe,Cr)_7C_3$ transforms into $(Fe,Cr)_{23}C_6$. XRD pattern of sample tempered at 873 K presents only ferrite peaks without austenite peak, probably because the austenite fraction is lower than 5%, which is known to be the average limit of detection by XRD [32]. Moreover, the dissolution of TiC is observed with the temperature increasing. According to Eq. 1 and CVF, the volume fractions (Table 3) of the retained austenite were obtained by calculating intensity of the $\alpha_{(110)}$ and $\gamma_{(111)}$. Additionally, the crystallite sizes of each phase (Table 4) were investigated.

Table 3 Temper effect on CVF as well as the volume fractions of the retained austenite and α-Fe/martensite

Tempered temperature	CVF (%)	V_γ (%)	$V_{\alpha/M}$ (%)
Untreated	3.20 ± 0.34	64.86 ± 0.06	31.94 ± 0.40
473 K	5.33 ± 0.77	52.93 ± 0.05	41.74 ± 0.83
673 K	2.25 ± 0.12	44.18 ± 0.04	53.57 ± 0.16
873 K	6.92 ± 0.31	<5	>87.77

Figure 6 is depicted based on the data from Tables 3 and 4, showing the austenite volume fraction and austenite crystallite size of different treatments. It indicates that with the tempering temperature increasing, both of them decline, attributed to the dissolving out of carbides and the transformation of austenite. Considering its evolution, it is noteworthy that the temperature ranging from 673 to 873 K is favorable for austenite transforming. The results were consisted with PARDAL's [26] work. Additionally, he/she pointed out the volume fraction was related to subsequent heat treatment time, which satisfied in an exponential function. According to the Hall–Petch relation, the refinement of the austenite after the tempering treatment might improve the mechanical properties of specimens. For instances, Ref. [34] reported that the carbon enriched

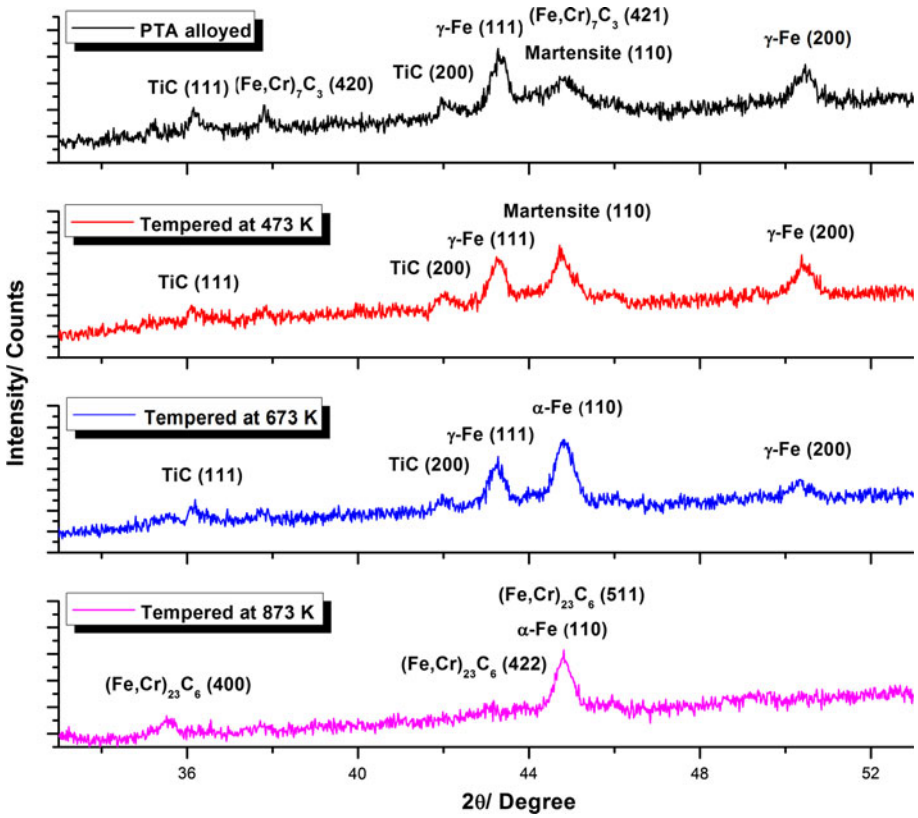

Fig. 5 X-ray diffraction pattern of AZ before and after tempering

Table 4 Temper effect on crystallite size (D_s) of different phases

Tempered temperature	γ-Fe		α/M	TiC	$(Fe,Cr)_{23}C_6$
	$D_{v(111)}$ (nm)	$D_{v(200)}$ (nm)	$D_{v(110)}$ (nm)	$D_{v(111)}$ (nm)	$D_{v(420)}$ (nm)
Untreated	25.21 ± 0.76	21.32 ± 0.64	12.19 ± 0.61	44.13 ± 2.21	–
473 K	15.85 ± 0.63	16.29 ± 0.65	15.96 ± 0.64	24.56 ± 0.73	–
673 K	10.57 ± 0.53	10.80 ± 0.54	21.17 ± 0.63	10.32 ± 0.52	18.21 ± 0.73
873 K	–	–	21.29 ± 0.64	–	24.29 ± 0.73

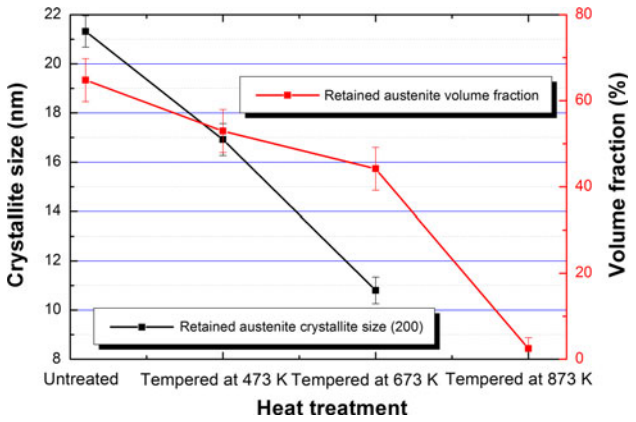

Fig. 6 Effect of tempering temperature on crystallite size and volume fractions of retained austenite

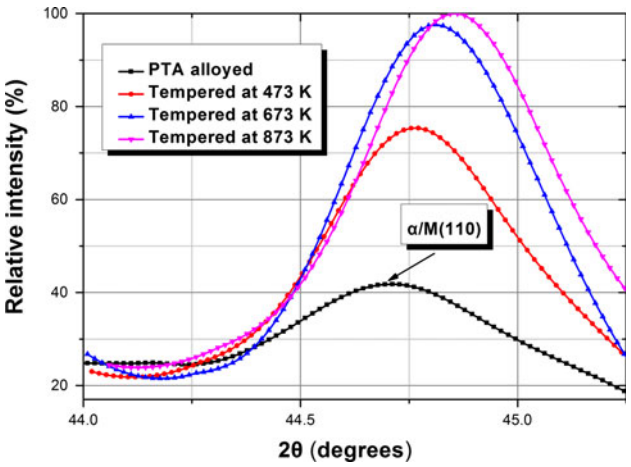

Fig. 7 Evolution of $\alpha/M_{(110)}$ peak in subsequent tempering

austenite which distributed uniformly tended to relax the stress of the crack tip and the refined microstructure of austenite could retard the propagation of fatigue cracks [35].

Figure 7 shows the effect of heat treatment temperature on the XRD profiles associated with the (110) reflections of α-Fe/martensite for samples. It indicates that the peak shifts towards high angles in a small way when the temperature rose from RT to 673 K. Reference [15] argued this phenomenon was related to the fact that tempered martensite evolved towards body centered cubic by the reduction of carbon content in solid solution. Furthermore, the reduction of peak width results in the increase of crystallite size [13, 28]. The increasing relative intensities of $\alpha/M_{(110)}$ peak also verified that the retained austenite trended to decrease with the heat treatment temperature elevation.

AZ's detailed microstructure of different heat treatments was examined by TEM. The typical bright-field images of PTA alloying and 473 K tempering are showed in Fig. 8a and b, respectively, presenting that the lath-like martensite within the retained austenite cell existed in the microstructure of the specimens; however, the lath-like martensite was not detected after 673 K subsequent tempering. It also shows that subsequent heat treatment exerts a remarkable effect on the lath thickness of the martensite. The width of the lath-like martensite formed after PTA alloying and 473 K subsequent tempering was measured at the random section. The results taken by approximately 20 times measurement were 38 ± 7 nm for non-subsequent heat treatment and 90 ± 10 nm for 473 K tempering. The formation of a coarser tempered martensitic structure within the retained austenite cell was caused by the fact that martensite plates began to grow in a high rate and nucleated with the temperature increased [36].

Effect of tempering temperature on microstructural development of HAZ

Figure 9 shows the HAZ microstructure of non-treatment and tempering treatment sample. After PTA alloying, the microstructure is mainly composed of martensite with some un-melted graphite (Fig. 9a). Comparing to a great quantity of austenite cell existing at the AZ, high proportion of martensite was in agreement with the previous work [1, 2, 37]. Liu [38] explained by the formation of the eutectic carbides in contact with the primary austenite at the AZ, which led to the excessive consumption and, as a result, depletion of C and Cr. Consequently, the M_s temperature dropped with the increase of distance from the bottom of the coating, causing the mass martensitic transformation. Tempered at 473 K resulted in in situ formation of temper pearlitic structure at the martensite plates (Fig. 9b), whereas further increased temperature to 673 K led martensite decompose (Fig. 9c). Figure 9d exhibited

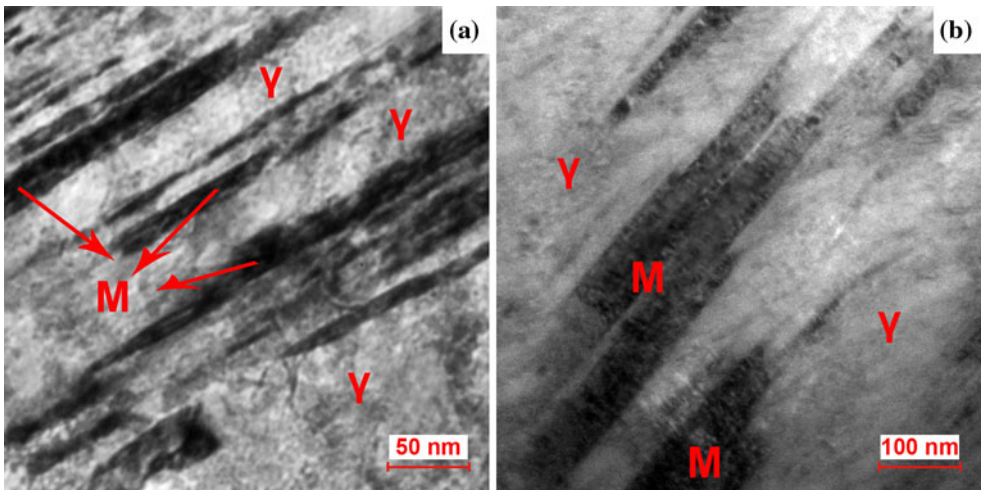

Fig. 8 TEM bright-field images of lath-like martensite of **a** PTA alloying and **b** 473 K tempering

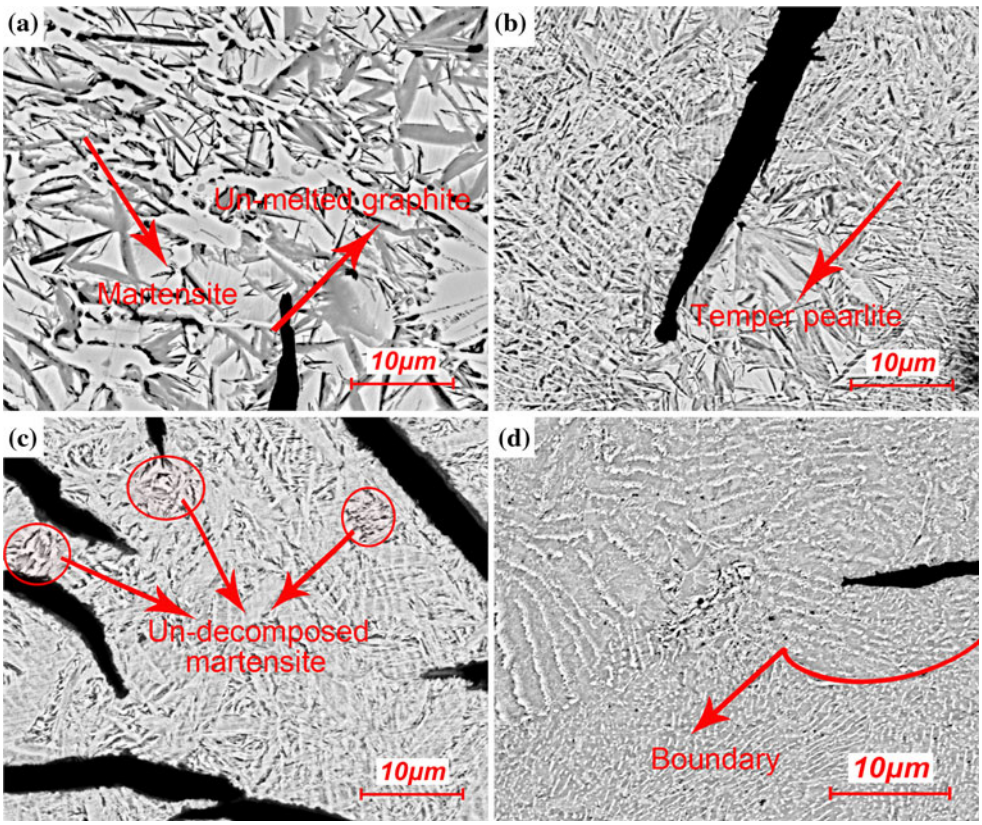

Fig. 9 Microstructure of HAZ: **a** PTA alloyed, **b** tempered at 473 K, **c** tempered at 673 K, **d** tempered at 873 K

the boundary of HAZ and matrix after 873 K treatment. Both regions showed a pearlitic structure; however, with a comparison, it was easy to find that temper pearlite of HAZ was much coarser. Additionally, after tempering, carbide in the ferrite phase or concentration of carbide at the grain boundaries, which had been reported in Ref. [21, 39], was not found in this study.

After obtaining the XRD pattern from the AZ, each specimen were ground by 0.3 mm from the surface layer, and then polished. To ensure that HAZ was exposed outside, the samples were observed in optical microscope before analyzing phase transformation of HAZ. The results were shown in Fig. 10, indicating that a large amount of martensite left at HAZ after PTA alloying; however, the

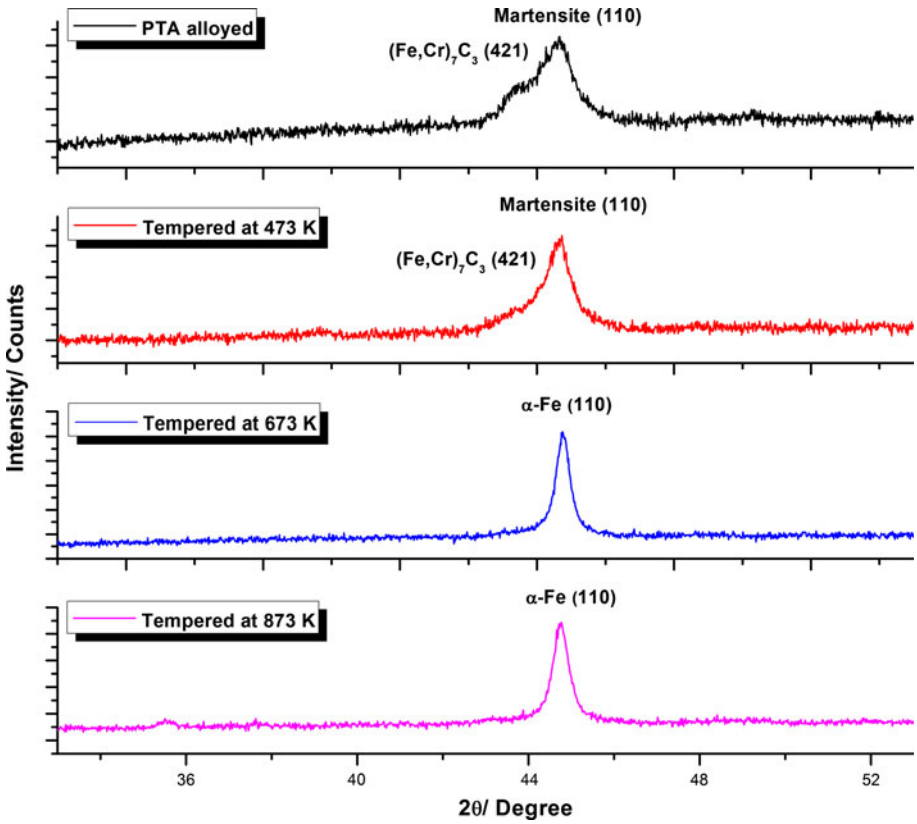

Fig. 10 X-ray diffraction pattern of HAZ before and after tempering

strongest diffraction peak of austenite at 43.47° was not observed. After tempering, the narrowing of diffraction line could be obviously seen. As we have known that the broadening of the diffraction peaks indicates the existence of the size effect and the strain effect (dislocation) [40–43], these effects are eliminated by heat treatment. According to Bello [42] and Pedro [44], the removal of the strain effect reduced the tensile residual stresses which existed at the overlap regions.

The variation of microhardness distribution affected by tempering temperature

Figure 11 depicts the microhardness distribution ranging from surface of the coatings to the gray cast iron before and after subsequent heat treatment. It can be seen that the microhardness distribution of the PTA alloying is different from the increased tempered temperatures. The maximum microhardness increased from 740 to 1310 HV at 473 K tempering; however, it decreased dramatically after temperature further increased. While increasing temperature, there are two effects completed with each other. On one hand, the increasing higher carbon martensite devotes to increasing hardness. On the other hand, the α-Fe content which forms in the higher temperatures tends to reduce hardness. In this study, the effect that 473 K tempered had a much higher microhardness at the surface than non-heat

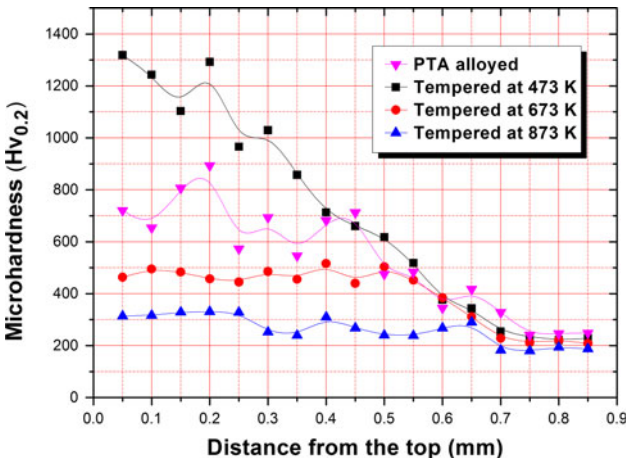

Fig. 11 Microhardness profile taken across of PTA alloying before and after tempering

treatment sample was mainly attributed to the increase of tempered martensite within γ-Fe in as well as the formation of the solid solution strengthening in the super-saturated γ-Fe solid solution (also seen Ref. [45]). After tempering at 673 K, the hardness profile was greatly below the untreated specimen, which must be contributed to the decomposition of tempered martensite and the transformation from the metastable high hardness $(Fe,Cr)_7C_3$ into stable $(Fe,Cr)_{23}C_6$. When tempered temperature increased to 873 K, the

retained austenite at the AZ was totally transformed into α-Fe and the HAZ was mainly composed of the tempered pearlite, therefore the microhardness showed the lowest.

Additionally, while the microhardness of the surface increased after tempered at 473 K, the microhardness of the matrix decreased from 245 to 220 HV, suggesting that alloying TiC–Cr could increase the softening resistance of the surface, which agreed with previous reported literatures [46, 47]. Zhang [47] claimed that the alloyed high entropy mixing can significantly lower the free energy; as a result, the diffusion coefficients and redistribution of the solute elements in subsequent heat treatment decreased. Consequently, even though the sluggish diffusion and segregation of solute elements, the TiC–Cr inevitably decreased the solubility and the AZ exhibited high softening resistance. Moreover, the microstructure variation along the depth of the hard layer as well as slight gradient of the microhardness is considered to be advantageous to the fatigue behavior of the matrix. For instances, it has been reported that the harden layer at the surface could protect the matrix from low-cycle fracture, improving the fatigue strength [48] and delaying fatigue crack initiation [49].

Weilbull distribution on fatigue life at different temper temperatures

Since Weibull distribution was being widely used to evaluate failure time and fracture strength in reliability engineering [50–52], in this study, the two-parameter Weibull distribution was employed to characterize differences between fatigue life predictions of PTA alloying and subsequent tempering treatment. The formula of probability density function in this case could be written as follows:

$$F(N) = 1 - \exp\left[-\left(\frac{N}{N_a}\right)^{\beta}\right] \tag{7}$$

where N, fatigue life failure cycles in this study; β, slope of Weibull distribution; N_a, characteristic life or scale parameter below which 63.2% of the data lie; $F(N)$, failure probability, given as $F(N) = i/(n + 1)$, suggested in Ref. [53].

The parameters of Weibull distribution and reliability analysis process were carried out by Origin 8.1 and the detailed procedures of calculation could be found in Ref. [52]. With the data, Fig. 12 was depicted, showing failure probability as a function of number of cycle to failure for PTA alloying before and after tempering specimens as well as matrix. And it demonstrated in the term of the statistical parentage of a specimen that had failed in the fatigue test. For instance, the life parameter, N_{90}, shown by a dash dot line in the Fig. 12, suggests the lifetime when 90% of specimens have experienced failure. Similarly, other life parameters, N_a, N_{10}, were depicted.

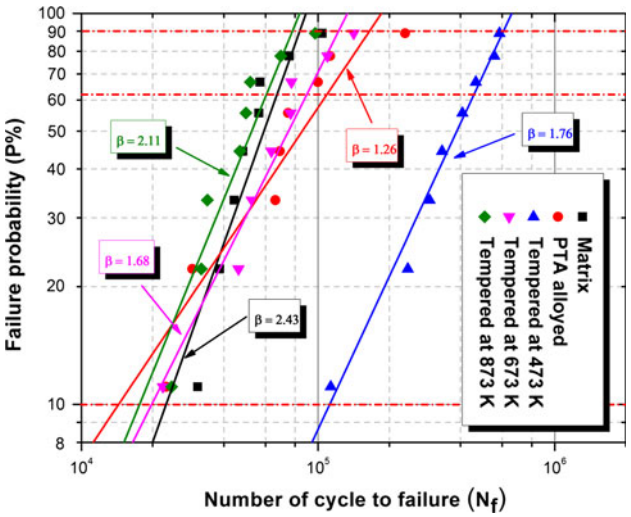

Fig. 12 Weibull distribution plots on fatigue life of PTA alloying before and after tempering as well as matrix

The results in Fig. 12 indicate that 473 K tempering significantly improved the fatigue life of alloying specimens; however, further elevation of the temperature directed fatigue strength degradation. Transformation of the microstructure and redistribution of the stress were attributed to this phenomenon. According to Bhambri work [54], the tempered martensitic structure had the highest resistance to fatigue crack growth followed in a decreasing order by tempered bainite, martensite, and ferrite–pearlite structures. On the other hand, after subsequent heat treatment, the residual stresses at the surface decreased, especially a majority of tensile residual stresses in the melted zone was eliminated [44, 55]. Moreover, there is a noticeable variation between the slope of data distribution, which is a measure of fatigue life dispersion, the larger the value of the parameter, the smaller the scatter of the fatigue life. Since the stress distribution at the crack tip is regarded as one of the determinative to the fatigue strength, tempering treatment benefits from alleviating its non-uniformity [35, 49, 54]; consequently, the fatigue life of tempering treated specimens becomes more predictable than the untreated specimens.

Conclusion

Appropriate subsequent heat treatment after PTA alloying could improve the microstructure and fatigue strength of the specimen. Based on analysis and discussion, the most significant results of this study are summarized as follows.

(1) After PTA alloying, the microstructure of AZ showed that it consisted of primary austenite, martensite, a

eutectic of $(Fe,Cr)_7C_3$ carbide and austenite as well as TiC. With the tempering temperature increasing, the tempered martensite was formed in the austenite cell, and the austenite was refined accompanied by transformation from $(Fe,Cr)_7C_3$ to $(Fe,Cr)_{23}C_6$ as well as dissolution of TiC.

(2) At HAZ, the microstructure PTA alloying produced was mainly composed of martensite with some unmelted graphite. After the tempering temperature increased, martensite gradually decomposed with the in situ the formation of coarser temper pearlitic structure. XRD suggested that the size effect and the strain effect were eliminated.

(3) 473 K temper after PTA alloying showed the highest microhardness; however, the microhardness decreased after temperature further increased

(4) While 473 K tempering could significantly improve the fatigue life of alloying specimens, further elevation of the temperature directed fatigue strength degradation. And tempering treatment improved distribution of fatigue life, making it less dispersed.

References

1. Bourithis L, Papaefthymiou S, Papadimitriou GD (2002) Appl Surf Sci 200:203
2. Ozel S, Kurt B, Somunkiran I, Orhan N (2008) Surf Coat Technol 202:3633
3. Sudha C, Shankar P, Subba Rao RV, Thirumurugesan R (2008) Surf Coat Technol 202:2103
4. Fallah V, Corbin SF, Khajepour A (2010) Surf Coat Technol 204:2400
5. Wang XH, Song SL, Qu SY, Zou ZD (2007) Surf Coat Technol 201:5899
6. Skarvelis P, Papadimitriou GD (2009) Surf Coat Technol 203:1384
7. Bourithis L, Papadimitriou GD (2009) Wear 266:1155
8. Jiang W, Molian P (2001) Surf Coat Technol 135:139
9. Gordani GR, ShojaRazavi R, Hashemi SH, Isfahani ARN (2008) Opt Laser Eng 46:550
10. Zhang Z, Ren L, Zhou H, Han Z, Tong X, Zhao Y, Chen L (2010) J Bionic Eng 7:390
11. Benyounis KY, Fakron OMA, Abboud JH, Olabi AG, Hashmi MJS (2005) J Mater Process Technol 170:127
12. Zhang L, Sun D, Yu H (2008) Mater Sci Eng A 490:57
13. Chowdhurya PS, Gayathria N, Mukherjeea P, Bhattacharyaa M, Chatterjeea A, Duttab A, Barat P (2011) Mater Sci Eng A 528:967
14. Korkut MH, Yilmaz O, Buytoz S (2002) Surf Coat Technol 157:5
15. Hoyosa JJ, Ghilarduccib AA, Salvab HR, Chavesa CA, Vélez JM (2011) Mater Sci Eng A 528:3385
16. Wang YD, Tang HB, Fang YL, Wang HM (2010) Mater Sci Eng A 528:474
17. Zhi X, Xing J, Gao Y, Hanguang F, Peng J, Xiao B (2008) Mater Sci Eng A 487:171
18. Beaurin G, Mathieu J-P, Gauthier E, Nelias D, Coret M, Arnoldi F (2011) Mater Sci Eng A 528:5096
19. Hua-yi L, Guo-lu L, Hai-dou W, Bin-shi X (2011) Mater Des 32:3004
20. Wu X, Hong Y (2000) Scripta Mater 43:123
21. Zhang L, Liu B, Yu H, Sun D (2007) Surf Coat Technol 201:5931
22. Wang Y, Li MY, Han B, Han T, Cheng YY (2010) J Mater Sci 45:3442. doi:10.1007/s10853-010-4371-1
23. Shi K, Hu S, Xu W, Huang Q (2010) Adv Mater Res 129–131:1109
24. Ji L, Hu S, Shi K, Huang Q, Xu W (2011) Heat Treat Met 36(6):7
25. ASTM E1245-03 Standard practice for determining the inclusion or second-phase constituent content of metals by automatic image analysis
26. Pardal JM, Tavares SSM, Cindra Fonseca MP (2006) J Mater Sci 41:2301. doi:10.1007/s10853-006-7170-y
27. De A, Murdock DC, Mataya MC, Speer JG, Matlock DK (2004) Scripta Mater 50:1445
28. Klug HP, Alexander LE (1974) X-ray diffraction procedures for polycrystalline and amorphous materials, 2nd edn. Wiley, New York
29. Lin YC, Wang SW (2004) Wear 256:720
30. Tabrett CP, Sare IR, Ghomashchi MR (1996) Int Mater Rev 41(2):52
31. Powell GLF, Bee JV (1996) J Mater Sci 31:707. doi:10.1007/BF00367889
32. Riber Miranda MA, Sasaki JM, Tavares SSM, de Abreu HFG, Neto JM (2005) Mater Charact 54:387
33. ASTM E562-08 Standard test method for determining volume fraction by systematic manual point count
34. Choi Y (2009) Int J Fatigue 31:1517
35. Guo YB, Barkey ME (2004) Int J Fatigue 26:605
36. Zhang P, Zhang FC, Wang TS (2011) Appl Surf Sci 257:7609
37. Nikolaou J, Bourithis L, Papadimitriou G (2003) J Mater Sci 38:2883. doi:10.1023/A:1024492720694
38. Liu Y-F, Han J-M, Li R-H, Li W-J, Xu X-Y, Wang J-H, Yang S-Z (2006) Appl Surf Sci 252:7539
39. Wu X, Chen G (1999) J Mater Sci 34:3355. doi:10.1023/A:1004676914422
40. Hanlon DN, Rainforth WM (2003) Wear 255:956
41. Li CG, Zhou QD, Song GS, Fang ZS (1993) Wear 162–164:75
42. Sun G, Zhang Y-k, Liu C, Luo K, Tao X, Li Peng (2010) Mater Des 31:2737
43. Bello JM, Fern BJ, Lopez V, Ruiz J (1994) J Mater Sci 29:5213. doi:10.1007/BF01151119
44. De la Cruz P, Oden M, Ericsson T (1998) Int J Fatigue 20(5):389
45. Zhang H, Cheng X, Bai B, Fang H (2011) Mater Sci Eng A 528:920
46. Lin C-M, Tsai H-L, Bor H-Y (2010) Intermetallics 18:1244
47. Zhang H, Pan Y, He YZ (2011) Surf Coat Technol 205:4068
48. Gonzalez-Hermosilla WA, Chicot D, Lesage J, La Barbera-Sosac JG, Gruescu IC (2010) Mater Sci Eng A 527:6551
49. Tsay LW, Liu YC, Lin D-Y, Young MC (2004) Mater Sci Eng A 328:177
50. Sivapragash M, Lakshminarayanan PR, Karthikeyan R, Raghukandan K, Hanumantha M (2008) Mater Des 29:1549
51. Shan D, Nayeb-Hashemi H (1999) NDT Int 32:265
52. Sakin R, Ay I (2008) Mater Des 29:1170
53. Ibrahim A, Berndt CC (2007) Mater Sci Eng A 456:114
54. Bhambri SK, Singh V, Jayaraman G (1989) Int J Fatigue 11(1):51
55. Tong X, Zhou H, Jiang W, Chen W, Li X, Ren L, Zhang Z (2009) Mater Sci Eng A 513–514:294